Evolution of the giant monopole resonance with triaxial deformation

Kouhei Washiyama [1,2,*] Shuichiro Ebata [3,†] and Kenichi Yoshida [1,4,5,‡]

[1]*Center for Computational Sciences, University of Tsukuba, Tsukuba, Ibaraki 305-8577, Japan*

[2]*Research Center for Superheavy Elements, Kyushu University, Fukuoka 819-0395, Japan*

[3]*Graduate School of Science and Engineering, Saitama University, Saitama 338-8570, Japan*

[4]*Research Center for Nuclear Physics, Osaka University, Ibaraki, Osaka 567-0047 Japan*

[5]*RIKEN Nishina Center for Accelerator-Based Science, Wako, Saitama 351-0198, Japan*

Background: The isoscalar giant monopole resonance (ISGMR) splits into two peaks in prolately deformed nuclei. When a nucleus is triaxially deformed, a peak appears in the middle between the two peaks.

Purpose: We investigate the mechanism of the appearance of the middle peak in the ISGMR in triaxial nuclei.

Method: We perform the constrained Skyrme-Hartree-Fock-Bogoliubov (CHFB) calculation for arbitrary triaxial shapes in ^{100}Mo. We calculate the strength functions of the isoscalar monopole (ISM) and IS quadrupole modes on the CHFB states. Furthermore, we investigate vibrations of matter distributions in x, y, and z directions induced by the external ISM field, with the z axis being the longest axis of the triaxial shape.

Results: The middle peak in the ISM strength evolves from the triaxial degree $\gamma = 0°$ to $60°$. This is because the difference between the vibration in the x direction and that in the y direction is evident with an increase in γ, and the quadrupole $K = 2$ component of the induced density of the ISM at the middle peak increases as γ increases, where K denotes the z component of the angular momentum. This property is also obtained in the unperturbed ISM strength without the residual fields.

Conclusions: The mixing between the monopole and quadrupole modes is primarily determined by the ground-state deformation. Therefore, the ISM strength of the middle peak becomes strong as the triaxial degree in the ground state increases.

I. INTRODUCTION

Understanding complex behaviors of atomic nuclei lies at the heart of low-energy nuclear physics. One of the central themes in this domain is the investigation of the collective modes exhibited in responses to nuclei. These collective modes play a pivotal role in elucidating the underlying structures and dynamics of nuclei, thereby providing crucial insights into their fundamental properties, such as nuclear shapes and deformations.

Giant resonances are a fundamental collective mode of excitation in nuclei [1]. It is well known that the isoscalar giant monopole resonance (ISGMR) splits into two peaks in prolately deformed nuclei [2]. This was first observed in the well-deformed ^{154}Sm nucleus [3]. Prior to this observation, the possible emergence of the two-peak structure in the IS-GMR strengths in deformed nuclei had been a subject of discussion [4]. Subsequently, it was found that the energy of the lower peak in the isoscalar monopole (ISM) strengths coincides with that of the $K = 0$ component of the isoscalar quadrupole (ISQ) strengths in prolately deformed nuclei,

where K denotes the z component of the angular momentum. Recent calculations based on the Hartree-Fock-Bogoliubov (HFB) method plus quasiparticle random-phase approximation (QRPA) in deformed nuclei confirmed this coincidence in energy [5–9].

Experimental identification of static triaxial deformations in nuclei can be achieved through various means, such as the observation of chiral doublet bands [10] and the wobbling mode, which was recently reported in ^{163}Lu [11]. In the low-lying spectra, the presence of the 2_2^+ state and the γ vibration provides evidence of a certain degree of triaxiality in nuclei. As a beyond mean-field method, the generator-coordinate method [12–16] and the collective Hamiltonian method [17–21] have included the triaxial degree of freedom as a collective coordinate and produced a better reproduction of experimental low-lying spectra. Besides that, it has been proposed that high-energy heavy-ion collisions can be used to extract information on triaxiality [22].

Recently, Shi and Stevenson [23] investigated the ISGMR in ^{100}Mo with the time-dependent density functional theory (TDDFT) + Bardeen-Cooper-Schrieffer (BCS) method with the Skyrme energy density functionals (EDFs). Then, they found that the calculation incorporating a triaxial shape ($\beta \approx 0.28$ and $\gamma = 20°$–$30°$) with the SkM* EDF opportunely reproduced the experimentally observed ISGMR at the Research Center for Nuclear Physics (RCNP), Osaka Univer-

*washiyama@nucl.ph.tsukuba.ac.jp

†ebata@mail.saitama-u.ac.jp

‡kyoshida@rcnp.osaka-u.ac.jp

sity [24]. Notably, the inclusion of finite triaxiality resulted in an increase in the ISM strength within the energy range of $E = 14$–15 MeV, making an additional peak between the two existing peaks and providing a closer match to the experimental data within that energy range. This observation serves as evidence of a static triaxial deformation ($\gamma = 20°$–30°) in ^{100}Mo. The authors further investigated variations in the isoscalar quadrupole moments over time subsequent to the ISM boost. They conjectured that the appearance of the middle peak is due to a coupling between the ISM and ISQ $K = 2$ modes and anticipated that, at triaxial shapes in the ground state, the external ISM field induces different vibrations in the three principal axes.

The operator of the ISM, $r^2 = x^2 + y^2 + z^2$, is isotropic. Nevertheless, the reason why the ISM external field induces anisotropic oscillations in deformed nuclei remains unclear. This study aims to explore the mechanism behind the emergence of the middle peak in the ISM strength and to elucidate the origin of anisotropic oscillations triggered by the isotropic ISM field in triaxially deformed nuclei. We perform the HFB + QRPA calculation to obtain the response function of the ISM for arbitrary triaxial shapes in ^{100}Mo. For the QRPA calculations, the finite amplitude method (FAM) [25] is used to provide the response function in a numerically feasible way. Then, we analyze the vibrations of matter distributions in the x, y, and z directions to delve into the underlying mechanisms contributing to the anisotropic oscillations induced by the ISM field.

The article is organized as follows. Section II describes the method of HFB + FAM-QRPA. In Sec. III, results of the ISM strengths in triaxial shapes and the analysis are presented. Finally, Sec. IV summarizes the present article.

II. METHOD

We briefly recapitulate the formulation of the constrained HFB (CHFB) + FAM-QRPA approach, and the details can be found in Refs. [7,25–28].

The FAM equation in the quasiparticle basis is given as

$$(E_\mu + E_\nu - \omega)X_{\mu\nu}(\omega) + \delta H_{\mu\nu}^{20}(\omega) = -F_{\mu\nu}^{20}, \quad (1a)$$

$$(E_\mu + E_\nu + \omega)Y_{\mu\nu}(\omega) + \delta H_{\mu\nu}^{02}(\omega) = -F_{\mu\nu}^{02}, \quad (1b)$$

where E_μ are the quasiparticle energies, X and Y are the FAM amplitudes at a given frequency ω, and $\delta H^{20(02)}$ and $F^{20(02)}$ are the two-quasiparticle components of an induced Hamiltonian and an external field $\hat{F}$, respectively. The FAM equation (1) can be solved iteratively at each ω by replacing ω with complex frequencies $\omega \to \omega + i\Gamma/2$, where the imaginary part Γ corresponds to a smearing width.

From the converged $X_{\mu\nu}(\omega; \hat{F})$ and $Y_{\mu\nu}(\omega; \hat{F})$ amplitudes induced by the external field $\hat{F}$, the FAM response function, the change of quantity associated with another field $\hat{F}'$ in the response to the perturbation $\hat{F}$, is defined as

$$R_{\hat{F}'\hat{F}}(\omega) = \sum_{\mu < \nu} \left[F_{\mu\nu}'^{20*} X_{\mu\nu}(\omega; \hat{F}) + F_{\mu\nu}'^{02*} Y_{\mu\nu}(\omega; \hat{F}) \right]. \quad (2)$$

Setting $\hat{F} = \hat{F}'$, the strength function is given as

$$S(\hat{F}; \omega) = -\frac{1}{\pi} \operatorname{Im} R_{\hat{F}\hat{F}}(\omega). \quad (3)$$

As an external field operator $\hat{F}$, we employ the one-body isoscalar monopole and quadrupole operators expressed as

$$f_{00} = \sum_{i=1}^{A} r_i^2, \quad f_{2K} = \sum_{i=1}^{A} r_i^2 Y_{2K}(\hat{r}_i). \quad (4)$$

We define the quadrupole operators with the x-signature quantum number of $r_x = \pm 1$ as $Q_{20}^{(+)} = f_{20}$ and $Q_{2K}^{(\pm)} = (f_{2K} \pm f_{2-K})/\sqrt{2}$ for $K > 0$. These quadrupole operators can also be expressed in terms of Cartesian coordinates as

$$Q_{20}^{(+)} = \sum_{i=1}^{A} \sqrt{\frac{5}{16\pi}} \left(2z_i^2 - x_i^2 - y_i^2 \right), \quad (5)$$

$$Q_{22}^{(+)} = \sum_{i=1}^{A} \sqrt{\frac{15}{16\pi}} \left(x_i^2 - y_i^2 \right). \quad (6)$$

We define the quadrupole deformation parameters β and γ as

$$\beta = \sqrt{\frac{5}{16\pi}} \frac{4\pi}{3R^2 A} \sqrt{\langle Q_{20}^{(+)} \rangle^2 + \langle Q_{22}^{(+)} \rangle^2}, \quad (7)$$

$$\gamma = \arctan\left(\frac{\langle Q_{22}^{(+)} \rangle}{\langle Q_{20}^{(+)} \rangle} \right), \quad (8)$$

where $R = 1.2A^{1/3}$ fm and A is the mass number. To investigate the evolution of the giant monopole resonance with triaxial deformation, we vary the triaxiality γ from $\gamma = 0°$ to $60°$, where $\gamma = 0°$ ($\gamma = 60°$) corresponds to the axially symmetric prolate (oblate) shape with the z axis (y axis) being a symmetry axis. In the region of $0° \leqslant \gamma \leqslant 60°$, the z and y axes are the longest and shortest axes, respectively.

To prepare triaxial CHFB states, we solve the Skyrme CHFB equations with the two-basis method [29,30] in a three-dimensional Cartesian mesh. The single-particle wave functions in the Hartree-Fock (HF) basis are chosen as eigenstates of parity, z signature, and y-time simplex [31–33]. With this choice, nuclear shapes are obtained with $x = 0$, $y = 0$, and $z = 0$ plane symmetries and the model space is reduced to $1/8$ of the full box. We use a $(13.2$ fm$)^3$ box in $x > 0$, $y > 0$, and $z > 0$ with a mesh spacing of 0.8 fm. The single-particle basis consists of 1400 neutron and 1120 proton HF-basis states, which approximately correspond to the maximum quasiparticle energy of 60 MeV. The constraint quantities are the isoscalar quadrupole moments with $K = 0$ and $K = 2$, $Q_{20}^{(+)}$ and $Q_{22}^{(+)}$. We employ the SkM* EDF [34] and the contact volume-type pairing with a pairing window of 20 MeV above and below the Fermi energy in the HF basis as described in Refs. [31,33,35]. The pairing strengths are adjusted to reproduce the empirical neutron and proton gaps in ^{106}Pd, and the resultant values are 240 MeV fm^3 and 285 MeV fm^3 for neutrons and protons, respectively. We confirmed that a change of the pairing strength of 5% does not affect the conclusions of this article.
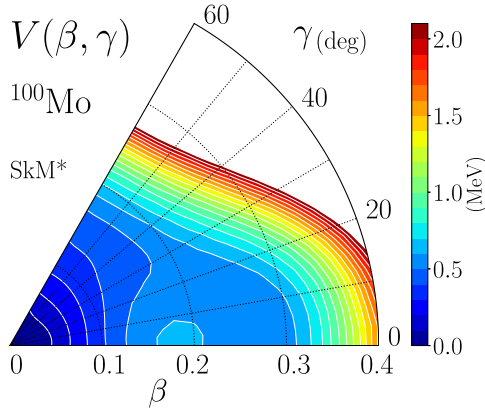
FIG. 1. Potential energy surface in the β-γ plane obtained by the CHFB calculation with the SkM* EDF in ^{100}Mo.

We perform the FAM-QRPA calculations at the CHFB states by using our 3D FAM-QRPA code developed in Ref. [27]. The full quasiparticle basis states that are included in solving the CHFB equation are used to solve the FAM equation (1). We solve the FAM equation at each ω up to $\omega = 40$ MeV with a spacing of 0.25 MeV and with a smearing width of $\Gamma/2 = 0.5$ MeV.

III. RESULTS AND DISCUSSION

Figure 1 shows the potential energy surface (PES) in the β-γ plane at $\beta < 0.4$ obtained by the CHFB calculation in ^{100}Mo. The PES shows the energy minimum at the spherical shape and a flat behavior along both the β and γ directions at $\beta \leqslant 0.3$. This behavior is consistent with that found in Ref. [23].

Given the γ-soft property of the PES in ^{100}Mo, our next step involves investigating the evolution of the ISGMR as the triaxiality parameter, γ, increases in ^{100}Mo. To accomplish this, we generate CHFB states at a fixed $\beta = 0.28$ with varying γ values and subsequently conduct FAM-QRPA calculations based on these prepared CHFB states. Figure 2(a) displays the ISM strength obtained by systematically altering γ in the FAM calculation on the CHFB states with $\beta = 0.28$ in ^{100}Mo. With $\gamma = 0$, we observe two prominent peaks at $\omega \approx 13$ MeV and at $\omega \approx 18$ MeV. As the value of γ increases, an additional peak emerges around $\omega = 15$ MeV, positioned between the existing lower and higher peaks. Furthermore, the strength of this middle peak exhibits a noticeable increase.

To understand the evolution of the middle peak with increasing γ, Fig. 2(b) presents the $K = 0$ and $K = 2$ components of the ISQ strength obtained by varying γ. The peak energy and its shape of the ISQ $K = 0$ strength do not much depend on γ, while the peak energy of the ISQ $K = 2$ strength decreases and its width becomes broader as γ increases. Notably, the peak energy of the ISQ $K = 2$ strength aligns with that of the middle peak in the ISM strength. This finding corroborates the results from a previous study [23], which demonstrated the appearance of an additional peak or plateau in the ISM strength at $\beta = 0.28$, $\gamma = 20°$ and $30°$ in ^{100}Mo
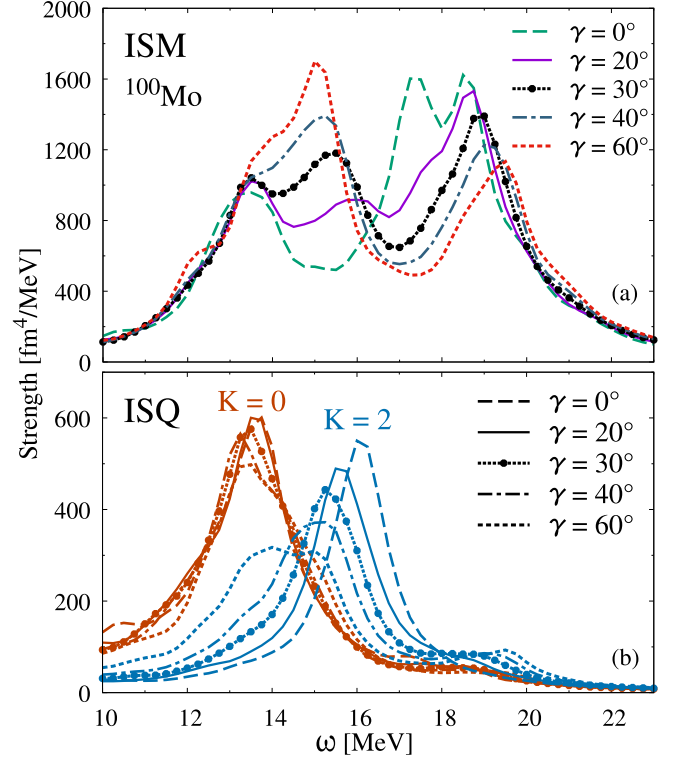

FIG. 2. (a) ISM strength and (b) ISQ strength as a function of ω for different γ in ^{100}Mo with $\beta = 0.28$.

using the SkM* EDF. Our results indicate that this coincidence persists for $\gamma > 30°$ as well.

To quantitatively observe the evolution of the middle peak in the ISM strength, we utilize the fraction of the energy-weighted sum rule (EWSR) value for the middle peak. We define the energy interval, denoted as E_1 and E_2, for the middle peak as follows: E_1 is set to be the average of the mean energies of the ISQ $K = 0$ and $K = 2$ strengths, and E_2 is the average of the mean energy of the ISQ $K = 2$ strength and the peak energy of the higher component in the ISM strength. Here, we determined the mean energy of the ISQ $K = 0$ and $K = 2$ using the expression:

$$E_{\text{mean}} = \frac{m_1}{m_0}, \tag{9}$$

where m_k is the kth moment of the strength function, defined as

$$m_k = \int_{\omega_1}^{\omega_2} d\omega\, \omega^k S(\omega), \tag{10}$$

where $\omega_1 = 10$ MeV and $\omega_2 = 23$ MeV determine the energy region of the giant resonance in this nucleus. The peak energy of the higher component in the ISM strength is determined by a Lorentzian fit. Figure 3 shows the fraction of the EWSR value for the middle peak in the ISM strength as a function of γ. It is clearly shown that the fraction of the EWSR value for the middle peak increases as γ increases up to $60°$. A similar behavior was obtained in a triaxial harmonic oscillator potential model in Ref. [36], where the ISGMR strength at the
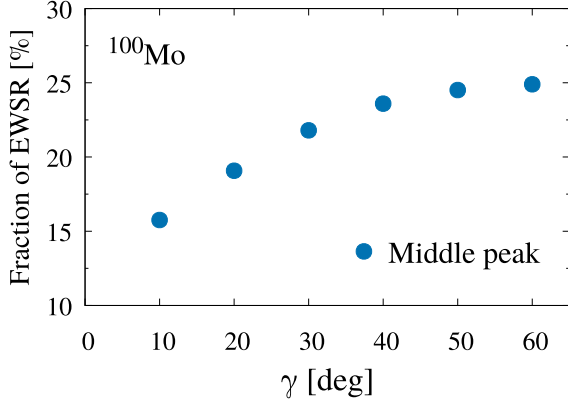
FIG. 3. Fraction of the EWSR value for the middle peak in the ISM strength as a function of γ.

middle peak monotonically increases as γ increases from $0°$ to $60°$.

We have obtained the emergence of the middle peak in the ISM strength and the agreement between the energy of the middle peak in the ISM strength and the peak energy of the ISQ $K = 2$ strength. The authors of Ref. [23] concluded that the appearance of the middle peak is attributed to a coupling between the ISM and ISQ $K = 2$ modes and anticipated that, at triaxial shapes with nonzero $\langle Q_{22}^{(+)} \rangle$, namely $\langle x^2 \rangle \neq \langle y^2 \rangle$, in the ground state, the external ISM field induces different vibrations in the x and y directions.

To see what really happens, we investigate vibrations of matter distributions in x, y, and z directions using an external ISM field that is isotropic. We calculate the FAM response function of $\hat{F}' = x^2$, y^2, or z^2 and the ISM field ($\hat{F} = \hat{r}^2$). Figure 4 shows the imaginary part of these response functions of the operators $\hat{F}$ and $\hat{F}'$,

$$S_{\hat{F}'\hat{F}}(\omega) = -\frac{1}{\pi} \operatorname{Im} R_{\hat{F}'\hat{F}}(\omega), \tag{11}$$

denoted as ISM $\to x^2$, ISM $\to y^2$, and ISM $\to z^2$, respectively, for different γ. It is noticed that the imaginary part of the response function (11) can be negative at particular values of ω since the product of the two-quasiparticle components of $\hat{F}$ and those of $\hat{F}'$ can be negative. Note again that a shape with $\langle z^2 \rangle \geqslant \langle x^2 \rangle \geqslant \langle y^2 \rangle$ is obtained at $0° \leqslant \gamma \leqslant 60°$ in our convention. At $\gamma = 0°$, the response of ISM $\to x^2$ is identical to that of ISM $\to y^2$ because of the axially symmetric shape. At $\omega \approx 13.5$ MeV, corresponding to the low peak in the ISM strength, the response of the ISM $\to z^2$ is significantly higher than those of ISM $\to x^2$ and ISM $\to y^2$. When the axial symmetry is broken, a discernible difference between those of ISM $\to x^2$ and ISM $\to y^2$ emerges, leading to a finite ISQ $K = 2$ strength, which is proportional to $x^2 - y^2$, induced by the ISM field. Furthermore, the peak energy of ISM $\to x^2$ becomes lower, and its response at $\omega \approx 15$ MeV, corresponding to the middle peak energy in the ISM strength, becomes higher while the response at $\omega \approx 18$ MeV decreases as γ increases from $0°$ to $60°$. For ISM $\to z^2$, the response at $\omega \approx 15$ MeV becomes higher while the response at $\omega \approx 13.5$ MeV becomes lower when γ increases from $0°$ to $60°$. At $\gamma = 60°$, the
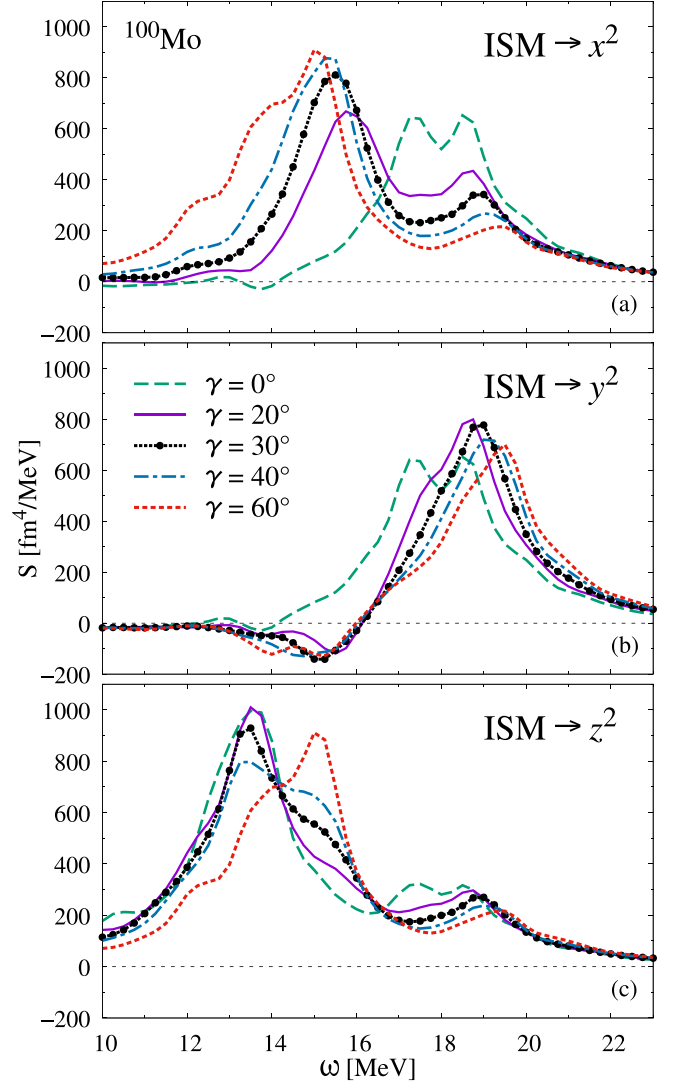

FIG. 4. Response functions of ISM $\to x^2$ (a), ISM $\to y^2$ (b), and ISM $\to z^2$ (c) for different γ in ^{100}Mo with $\beta = 0.28$.

response of the ISM $\to x^2$ is identical to that of ISM $\to z^2$ due to the axially symmetric shape with the y being the symmetry axis.

The response function in Eq. (11) is related to the Fourier transform of vibrations of matter distributions in x, y, and z directions induced by the ISM field. At $\gamma = 0°$, since the response of ISM $\to x^2$ and that of ISM $\to y^2$ are the same, the vibration of matter distributions in the x direction and that in the y direction are the same. Since the response of ISM $\to z^2$ and that of ISM $\to x^2$ and ISM $\to y^2$ are different, the vibration of matter distributions in the z direction and that in the x and y directions are different in $\gamma = 0°$. As γ increases, the vibrations of matter distributions in x, y, and z directions become different. Eventually, at $\gamma = 60°$, the responses of ISM $\to x^2$ and ISM $\to z^2$ become identical, indicating that the vibration of matter distributions in x and that in z become identical. The external multipole fields F_L that we have employed are rotational-invariant. The breaking of the spherical symmetry in the ground state density manifests the
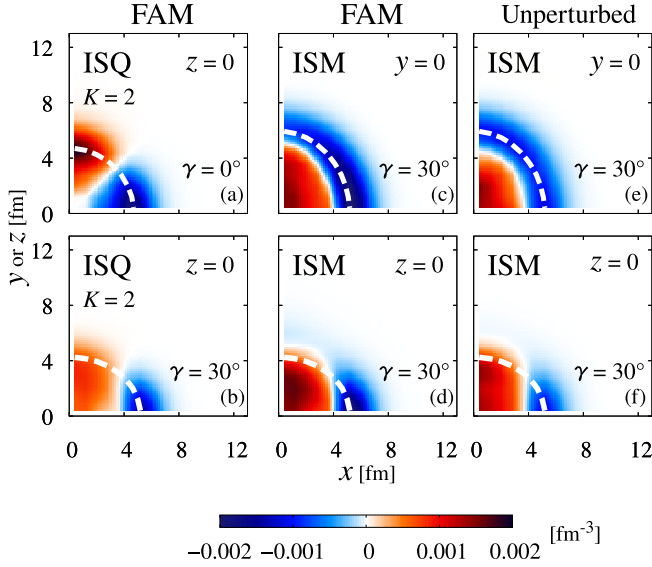
FIG. 5. Induced densities for the ISQ $K = 2$ field at $\omega = 16$ MeV on the $z = 0$ plane at $\gamma = 0°$ (a) and $\gamma = 30°$ (b), and for the ISM field at $\omega = 16$ MeV on the $y = 0$ (c) and $z = 0$ (d) planes and induced densities without the residual ISM field at $\omega = 20$ MeV on the $y = 0$ (e) and $z = 0$ (f) planes at $\gamma = 30°$ in ^{100}Mo. The dashed line indicates the contour of the isoscalar density $\rho = 0.08$ fm^{-3} obtained by the CHFB calculation at $\gamma = 30°$, except for (a) at $\gamma = 0°$.

FIG. 6. $L = 2$, $K = 2$ component of the induced density by the ISM field for different γ. The nuclear radius is indicated in the arrow. The $L = 0$ component of the induced density at $\gamma = 30°$ is plotted by the dotted line.

asymmetry of the strengths in F_L with respect to x, y, and z directions.

To understand how the ISM field induces a significant contribution of quadrupole vibrations, it is useful to analyze the spacial property of the induced density of the collective states. The induced density at a frequency ω in the FAM is obtained with the FAM X and Y amplitudes as

$$\delta\rho(\boldsymbol{r};\omega) = \sum_{ij} \phi_i(\boldsymbol{r})[UX(\omega)V^T + V^*Y^T(\omega)U^\dagger]_{ij}\phi_j^*(\boldsymbol{r}),$$

(12)

where U and V are the Bogoliubov transformation matrices and $\phi_i(\boldsymbol{r})$ are the HF basis wave functions. Figures 5(c) and 5(d) show the imaginary part of the induced density on the $y = 0$ and $z = 0$ planes, respectively, by the ISM field at $\omega = 16$ MeV, which approximately corresponds to the energy of the middle peak in the ISM strength, at $\gamma = 30°$, $\beta = 0.28$ in ^{100}Mo. The dashed line indicates the contour of the isoscalar density $\rho = 0.08$ fm^{-3} of this nucleus obtained by the CHFB calculation. The induced density on the $y = 0$ plane (c) shows that the density becomes higher inside the nucleus and lower at the nuclear surface, and shows almost an isotropic nature. On the other hand, the induced density on the $z = 0$ plane (d) shows an anisotropic nature. The induced density has a node along the x direction and becomes higher at smaller x and lower at larger x. This spacial property of the induced density resembles that in the $K = 2$ field of the quadrupole vibration mode, which is shown in Fig. 5(b). For comparison,
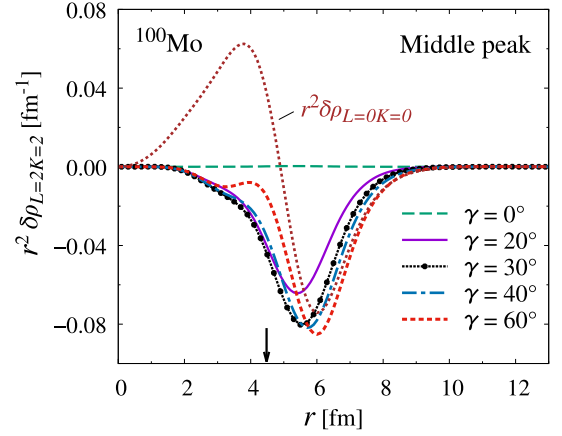
the induced density for the ISQ $K = 2$ at $\gamma = 0°$ is shown in (a), which has a node along $x = y$.

We go through the property of the induced density at the middle peak. We show in Fig. 6 the $L = 2$, $K = 2$ component of the induced density of the ISM field for different γ obtained by the multipole expansion of the induced density of the ISM field. To see the surface property of the induced density, we plot the induced density multiplied by r^2 in the figure. The $L = 2$, $K = 2$ component of the induced density vanishes for the axially symmetric case ($\gamma = 0°$). The magnitude of the $L = 2$, $K = 2$ component at the surface becomes larger for larger γ. For comparison, we plot the $L = 0$ component of the induced density at $\gamma = 30°$ as the dotted line. Its magnitude at the surface region is comparable to that in the $L = 2$, $K = 2$ component at $\gamma = 20°$, $30°$, $40°$, and $60°$. This clearly shows a strong mixing of the $L = 2$, $K = 2$ component of the ISM strength at the middle peak energy.

To ascertain whether the origin of the $L = 2$, $K = 2$ component of the ISM strength stems from either dynamical effect or static effect, we also look into the ISM strength without the residual fields in the FAM calculation, namely the unperturbed strength. Figure 7 shows the unperturbed ISM and ISQ strengths at different γ. The occurrence of the middle peak in the unperturbed ISM strength at finite γ is seen at $\omega \approx 20$ MeV. Furthermore, the middle peak in the unperturbed ISM strength and the peak in the unperturbed ISQ $K = 2$ strength coincide in energy. These properties are preserved when the residual effects are taken into account, which we have seen in Fig. 2. A similar feature has been pointed out in the case of the isovector monopole excitations in axially deformed nuclei [37]. In addition to this, as shown in Figs. 5(e) and 5(f), the spacial property of the induced density without the residual fields is almost the same as that with the residual fields shown in Figs. 5(c) and 5(d). From this analysis, the triaxial deformation in the ground state density induces significant contribution of $L = 2$, $K = 2$ component to the ISM strength.
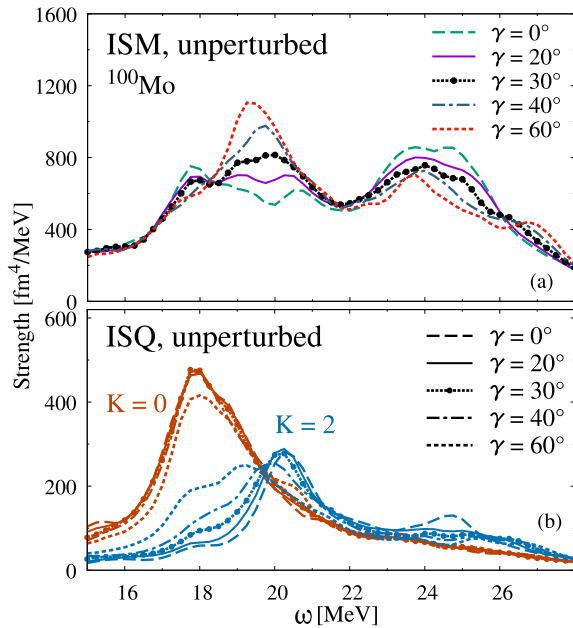
FIG. 7. Same as Fig. 2, but for the unperturbed strength.

IV. SUMMARY

We have investigated the mechanism underlying the emergence of the middle peak in the ISM strengths in deformed nuclei breaking the axial symmetry. We performed the CHFB + FAM-QRPA calculations to obtain the ISM and ISQ strengths in the ^{100}Mo nucleus, where the triaxial deformation has been pointed out to appear. The evolution of the middle peak in the ISM strength is clearly shown in the analysis of the fraction of the EWSR value. We also investigated the vibrations of matter distributions in the x, y, and z directions by the ISM field and found that the origin of the middle peak in the ISM strength is due to different vibrations of matter distributions in the x and y directions with $\gamma > 0°$. The induced density of the ISM field possesses an enhanced $L = 2$, $K = 2$ component with $\gamma > 0°$ at the middle-peak energy. Additionally, we have conducted similar calculations for the case without the residual ISM field and found the occurrence of the middle peak in the unperturbed ISM strength as well as the mixing of the $L = 2$, $K = 2$ component to the ISM strength at the middle peak energy. The mixing between the monopole and quadrupole modes is given by the ground state deformation. Therefore, the ISM strength of the middle peak becomes strong as γ increases.

[1] M. Harakeh and A. Woude, *Giant Resonances: Fundamental High-frequency Modes of Nuclear Excitation* (Oxford University Press, Oxford, 2001).

[2] U. Garg and G. Colò, The compression-mode giant resonances and nuclear incompressibility, Prog. Part. Nucl. Phys. **101**, 55 (2018).

[3] U. Garg, P. Bogucki, J. D. Bronson, Y. W. Lui, C. M. Rozsa, and D. H. Youngblood, Splitting of the giant monopole resonance with deformation in Sm nuclei, Phys. Rev. Lett. **45**, 1670 (1980).

[4] D. Zawischa, J. Speth, and D. Pal, Low- and high-energy collective states of deformed nuclei, Nucl. Phys. A **311**, 445 (1978).

[5] K. Yoshida, Collective modes of excitation in deformed neutron-rich Mg isotopes, Mod. Phys. Lett. A **25**, 1783 (2010).

[6] K. Yoshida, Roles of deformation and neutron excess on the giant monopole resonance in neutron-rich Zr isotopes, Phys. Rev. C **82**, 034324 (2010).

[7] T. Nikšić, N. Kralj, T. Tutiš, D. Vretenar, and P. Ring, Implementation of the finite amplitude method for the relativistic quasiparticle random-phase approximation, Phys. Rev. C **88**, 044327 (2013).

[8] J. Kvasil, V. O. Nesterenko, A. Repko, W. Kleinig, and P.-G. Reinhard, Deformation-induced splitting of the isoscalar *E*0 giant resonance: Skyrme random-phase-approximation analysis, Phys. Rev. C **94**, 064302 (2016).

[9] X. Sun and J. Meng, Finite amplitude method on the deformed relativistic Hartree-Bogoliubov theory in continuum: The isoscalar giant monopole resonance in exotic nuclei, Phys. Rev. C **105**, 044312 (2022).

[10] S. Frauendorf and Jie Meng, Tilted rotation of triaxial nuclei, Nucl. Phys. A **617**, 131 (1997).

[11] S. W. Ødegård, G. B. Hagemann, D. R. Jensen, M. Bergström, B. Herskind, G. Sletten, S. Törmänen, J. N. Wilson, P. O. Tjøm, I. Hamamoto, K. Spohr, H. Hübel, A. Görgen, G. Schönwasser, A. Bracco, S. Leoni, A. Maj, C. M. Petrache, P. Bednarczyk, and D. Curien, Evidence for the wobbling mode in nuclei, Phys. Rev. Lett. **86**, 5866 (2001).

[12] M. Bender and P.-H. Heenen, Configuration mixing of angular-momentum and particle-number projected triaxial Hartree-Fock-Bogoliubov states using the Skyrme energy density functional, Phys. Rev. C **78**, 024309 (2008).

[13] T. R. Rodríguez and J. L. Egido, Triaxial angular momentum projection and configuration mixing calculations with the Gogny force, Phys. Rev. C **81**, 064323 (2010).

[14] J. M. Yao, J. Meng, P. Ring, and D. Vretenar, Configuration mixing of angular-momentum-projected triaxial relativistic mean-field wave functions, Phys. Rev. C **81**, 044311 (2010).

[15] M. Kimura, Y. Taniguchi, Y. Kanada-En'yo, H. Horiuchi, and K. Ikeda, Prolate, oblate, and triaxial shape coexistence, and the lost magicity of $N = 28$ in ^{43}S, Phys. Rev. C **87**, 011301(R) (2013).

[16] Y. Suzuki and M. Kimura, Triaxial deformation and the disappearance of the $N = 28$ shell gap, Phys. Rev. C **104**, 024327 (2021).

[17] J. Libert, M. Girod, and J.-P. Delaroche, Microscopic descriptions of superdeformed bands with the Gogny force: Configuration mixing calculations in the $A \sim 190$ mass region, Phys. Rev. C **60**, 054301 (1999).

[18] L. Próchniak, P. Quentin, D. Samsoen, and J. Libert, A self-consistent approach to the quadrupole dynamics of medium heavy nuclei, Nucl. Phys. A **730**, 59 (2004).

[19] T. Nikšić, Z. P. Li, D. Vretenar, L. Próchniak, J. Meng, and P. Ring, Beyond the relativistic mean-field approximation. III. Collective Hamiltonian in five dimensions, Phys. Rev. C **79**, 034303 (2009).

[20] K. Matsuyanagi, M. Matsuo, T. Nakatsukasa, K. Yoshida, N. Hinohara, and K. Sato, Microscopic derivation of the Bohr-Mottelson collective Hamiltonian and its application to quadrupole shape dynamics, Phys. Scr. **91**, 063014 (2016).

[21] K. Washiyama and K. Yoshida, Triaxial-shape dynamics in the low-lying excited 0^+ state: Role of the collective mass, Phys. Rev. C **108**, 014323 (2023).

[22] J. Jia, Probing triaxial deformation of atomic nuclei in high-energy heavy ion collisions, Phys. Rev. C **105**, 044905 (2022).

[23] Y. Shi and P. D. Stevenson, Isoscalar monopole strength in ^{100}Mo: an indicator for static triaxial deformation in the ground state, Chin. Phys. C **47**, 034105 (2023).

[24] K. Howard, U. Garg, M. Itoh, H. Akimune, M. Fujiwara, T. Furuno, Y. Gupta, M. Harakeh, K. Inaba, Y. Ishibashi, K. Karasudani, T. Kawabata, A. Kohda, Y. Matsuda, M. Murata, S. Nakamura, J. Okamoto, S. Ota, J. Piekarewicz, A. Sakaue *et al.*, Compressional-mode resonances in the molybdenum isotopes: Emergence of softness in open-shell nuclei near A = 90, Phys. Lett. B **807**, 135608 (2020).

[25] T. Nakatsukasa, T. Inakura, and K. Yabana, Finite amplitude method for the solution of the random-phase approximation, Phys. Rev. C **76**, 024318 (2007).

[26] M. Stoitsov, M. Kortelainen, T. Nakatsukasa, C. Losa, and W. Nazarewicz, Monopole strength function of deformed superfluid nuclei, Phys. Rev. C **84**, 041305(R) (2011).

[27] K. Washiyama and T. Nakatsukasa, Multipole modes of excitation in triaxially deformed superfluid nuclei, Phys. Rev. C **96**, 041304(R) (2017).

[28] K. Washiyama, N. Hinohara, and T. Nakatsukasa, Finite-amplitude method for collective inertia in spontaneous fission, Phys. Rev. C **103**, 014306 (2021).

[29] B. Gall, P. Bonche, J. Dobaczewski, H. Flocard, and P.-H. Heenen, Superdeformed rotational bands in the mercury region. A cranked Skyrme-Hartree-Fock-Bogoliubov study, Z. Phys. A **348**, 183 (1994).

[30] J. Terasaki, P.-H. Heenen, P. Bonche, J. Dobaczewski, and H. Flocard, Superdeformed rotational bands with density dependent pairing interactions, Nucl. Phys. A **593**, 1 (1995).

[31] P. Bonche, H. Flocard, P.-H. Heenen, S. J. Krieger, and M. S. Weiss, Self-consistent study of triaxial deformations: Application to the isotopes of Kr, Sr, Zr and Mo, Nucl. Phys. A **443**, 39 (1985).

[32] J. Dobaczewski, J. Dudek, S. G. Rohoziński, and T. R. Werner, Point symmetries in the Hartree-Fock approach. I. Densities, shapes, and currents, Phys. Rev. C **62**, 014310 (2000).

[33] W. Ryssens, V. Hellemans, M. Bender, and P.-H. Heenen, Solution of the Skyrme-HF+BCS equation on a 3D mesh, II: A new version of the Ev8 code, Comput. Phys. Commun. **187**, 175 (2015).

[34] J. Bartel, P. Quentin, M. Brack, C. Guet, and H.-B. Håkansson, Towards a better parametrisation of Skyrme-like effective forces: A critical study of the SkM force, Nucl. Phys. A **386**, 79 (1982).

[35] C. Rigollet, P. Bonche, H. Flocard, and P.-H. Heenen, Microscopic study of the properties of identical bands in the $A = 150$ mass region, Phys. Rev. C **59**, 3120 (1999).

[36] Y. R. Shimizu and K. Matsuyanagi, Monopole and quadrupole giant resonances in rotating triaxially deformed nuclei, Prog. Theor. Phys. **72**, 1017 (1984).

[37] K. Yoshida, Isovector giant monopole and quadrupole resonances in a Skyrme energy density functional approach with axial symmetry, Phys. Rev. C **104**, 044309 (2021).